Pacific Northwest
NATIONAL LABORATORY

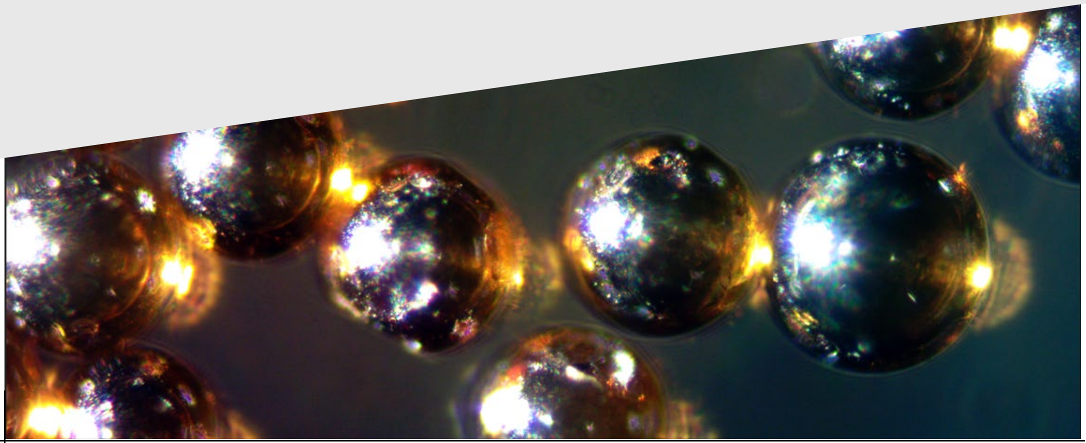

PNNL-36818

Metallic Coating of Cerium Oxide Microspheres

September 2024

Lance Hubbard
Christina Arendt
Gregory Dindlebeck
Brittany Robertson
Sarah Miley
Clara Reed
Dion Sunderland
Mark Engelhard
Jeff Katalenich

U.S. DEPARTMENT OF ENERGY

Prepared for the U.S. Department of Energy
under Contract DE-AC05-76RL01830

PACIFIC NORTHWEST NATIONAL LABORATORY
operated by
BATTELLE
for the
UNITED STATES DEPARTMENT OF ENERGY
under Contract DE-AC05-76RL01830

Printed in the United States of America

Available to DOE and DOE contractors from
the Office of Scientific and Technical Information,
P.O. Box 62, Oak Ridge, TN 37831-0062
www.osti.gov
ph: (865) 576-8401
fox: (865) 576-5728
email: reports@osti.gov

Available to the public from the National Technical Information Service
5301 Shawnee Rd., Alexandria, VA 22312
ph: (800) 553-NTIS (6847)
or (703) 605-6000
email: info@ntis.gov
Online ordering: http://www.ntis.gov

PNNL-36818

Metallic Coating of Cerium Oxide Microspheres

September 2024

Lance Hubbard
Christina Arendt
Gregory Dindlebeck
Brittany Robertson
Sarah Miley
Clara Reed
Dion Sunderland
Mark Engelhard
Jeff Katalenich

Prepared for
the U.S. Department of Energy
under Contract DE-AC05-76RL01830

Pacific Northwest National Laboratory
Richland, Washington 99354

Abstract

The ability to remove heat is paramount to nuclear fuel performance and longevity. Retaining fission product and separating fuel from reactor coolant and the environment is also necessary to prevent radiological contamination. Conventional nuclear fuel for commercial light water reactors and radioisotope power systems (RPS) is composed of oxide powders pressed into a pellet (cm-scale) and then sealed into a metal cladding to confine the fuel. What typical fuels lack is a method to surround each particle of nuclear fuel in metal, thus providing a more intimate protection layer for accident tolerance and boosting the thermal extraction from the fuel element. In such a way, metal-coated fuel particles increase heat extraction efficiency over clad-pellet designs while increasing the accident tolerance of the fuel. Metal oxide microspheres have wide-ranging applications, including the realm of fuels for nuclear reactors and RPS. Microspheres of uranium oxide/uranium carbide, mixed uranium/plutonium oxides, transuranics, and thorium fuels have been extensively studied. Pacific Northwest National Laboratory has also demonstrated the production of $^{238}PuO_2$ microspheres for RPS applications. Metal-coated oxide microsphere fuels may also be attractive for other applications such as nuclear thermal rockets, future nuclear reactor designs, and catalysts.

Keywords

Core-shell, nuclear fuel, coating, fuel development, coated particle, accident tolerant, polyol reduction

Graphical Abstract

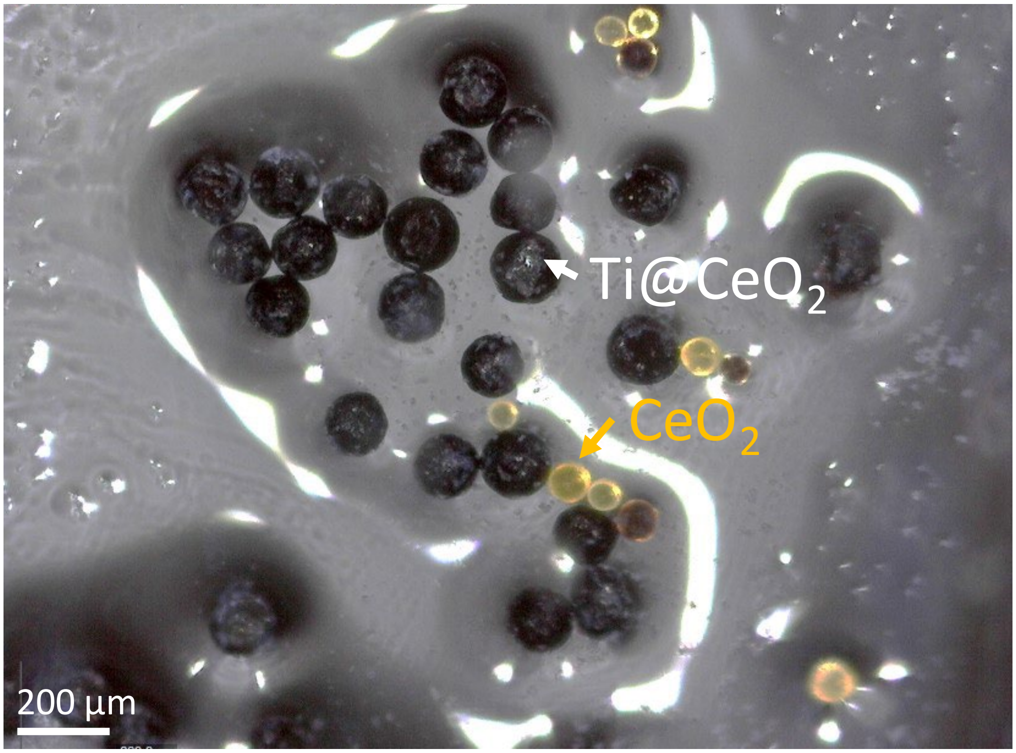

Acknowledgments

This research was supported by the Strategic Investments Initiative, under the Laboratory Directed Research and Development Program at Pacific Northwest National Laboratory (PNNL). PNNL is a multi-program national laboratory operated for the Department of Energy by Battelle Memorial Institute under Contract No. DE-AC05-76RL01830.

Conflict of Interest Statement

On behalf of all authors, the corresponding author states that there is no conflict of interest.

Data Availability Statement

The datasets generated during and/or analyzed during the current study are available from the corresponding author upon reasonable request.

Author Contributions

Lance Hubbard designed the experiments and procedures, performed the optical analysis, and oversaw the writing. Christina Arendt adjusted the procedures and performed the coating experiments. Brian Dindlebeck and Clara Reed performed the statistical particle sizing. Sarah Miley performed the literature survey. Dion Sunderland performed the selection of the materials. Mark Englemann performed the XPS analysis. Finally, Jeff Katalenich was the project manager and provided microsphere samples for coating experiments.

Contents

Figures

Tables

1.0 Introduction

The ability to remove heat is paramount to nuclear fuel performance and longevity (Harp et al. 2015). Conventional nuclear fuel for commercial light water reactors and radioisotope power systems (RPS) is composed of oxide powders pressed into a pellet (cm-scale) and then sealed into a metal cladding to confine the fuel (Clark et al. 2007). What typical fuels lack is a method to surround each particle of nuclear fuel in metal, thus providing a more intimate protection layer for accident tolerance and boosting the thermal extraction from the fuel element. In such a way, metal-coated fuel particles increase heat extraction efficiency over clad-pellet designs while increasing the accident tolerance of the fuel. Metal oxide microspheres have wide-ranging applications, including the realm of fuels for nuclear reactors and RPS. Microspheres of uranium oxide/uranium carbide, mixed uranium/plutonium oxides, transuranics, and thorium fuels have been extensively studied. PNNL has also demonstrated the production of $^{238}PuO_2$ microspheres for RPS applications. Metal-coated oxide microsphere fuels may also be attractive for other applications such as nuclear thermal rockets and future nuclear reactor designs.

Sol-gel approaches are an attractive means to produce high-quality uniform microspheres for nuclear fuels (Katalenich et al. 2018). Internal gelation sol-gel methods (which create pure metal oxide spheres out of aqueous metal nitrate solutions) were originally developed to produce uranium oxide microspheres for advanced tri-structural isotropic (TRISO) nuclear fuels. Microspheres of uranium, thorium, and cerium oxides (as a surrogate for PuO_x) (Arima et al. 2005) have all been successfully produced via sol-gel methods and continue to be studied for their applications to nuclear fuels (Brykala and Rogowski 2016; Maji et al. 2023; Suresh Kumar et al. 2003). These sol-gel methods are advantageous because solid gels are formed from aqueous solutions during internal gelation, causing final products to exhibit a homogeneous distribution of elements dissolved in the feed solution (J. A. Katalenich et al., 2018; J. Katalenich & Sholtis, 2021; Sawant et al., 2002; Vaidya et al., 1987). Sol-gel microsphere production is also essentially dust-free compared to traditional, powder-based fuel fabrication (Aegerter et al. 2011). In particular, recent studies of sol-gel CeO_x production show excellent purity comparisons to commercial powder CeO_x standards (Sökücü et al. 2015). Sol-gel microsphere fuels may be pressed into pellets or loaded into a cladding and vibro-compacted, but present challenges with heat conduction and dispersibility in an accident scenario. The addition of a noble metal coating alleviates these challenges by providing a thermally conductive barrier layer (Clavier et al. 2017; Hao et al. 2014; Katalenich and Sholtis 2021; Matthews and Hart 1980; Somayajulu 2017).

Related to sol-gel reduction for oxides is the polyol reduction for metals. Typically, this method is used to create engineered metal nanoparticles (Carroll et al. 2011; Fievet et al. 2018; Ma et al. 2016). It has been shown that with the use of functionalization (Park et al. 2006) the polyol method can be extended to coat oxide surfaces with nanometers to microns of metal (Hubbard 2016). By applying the functionalization and coating processes demonstrated (Hubbard 2016) with sol-gel proceeded fuels, we sought to demonstrate that each fuel particle can be coated in an inert metal. Specifically, we hypothesized that a 10-micron thick iridium-coated sphere of cerium oxide that has been fired in air to 1,000°C for 2 hours will have only marginal (within the detection limit error) leakage of the cerium core when suspended in pure methanol at ambient temperatures for 72 hours. By showing that these coated cerium oxide particles do not dissolve when leach tested, we have demonstrated the individually coated fuel particles can be created by modification of the polyol process and that they have the potential to increase fuel accident tolerance and thermal extraction efficiency.

1.1 Precious Metal Group Materials & Alloy Selection

For coated particles of an alpha-emitting thermal source, e.g., $^{238}PuO_2$, stopping alpha particles within 10 to 15 microns of the surface of the source can be accomplished with Ir or Pt. Iridium has the benefit of being more oxidation-resistant, having a higher thermal conductivity, and having greater strength. An additional layer of a lighter Mo-alloy, e.g., Mo-5%Re could also be applied.

For high-temperature nuclear reactor fuel, the coating must be compatible with whatever form will be used for the fuel: UO_2, UMo, UZr, UC, or UN. Uranium nitride is desirable for its higher thermal conductivity and low fission gas release; however, at very high temperature and with irradiation, free nitrogen becomes available and would chemically interact with the cladding. Rhenium (Re) has been proposed as a coating, but a precious metal group coating may also be applied, possibly to the ceramic fuel particles. The coating should be as thin as possible, and also be compatible with the cladding material, which would likely be a material with minimal parasitic neutron absorption (Klopp 1985).

For catalytic systems, the coatings may be a combination of precious group metals depending on the desired reaction. There would likely be a base material to provide a relatively large surface area, with a base catalyst, or a temperature-/corrosion-resistant coating, then an active catalyst of a given precious group metal or a combination of precious metal groups, e.g., Pt/Pd with Rh/Ru, depending on the desired synthesis.

Overall, the following rankings can be made:

1) Ranked by melting point: W, Re, Os, Ta, Mo, Nb, Ir
2) Ranked by thermal conductivity: W, Rh, Ir, Mo, Ru
3) Ranked by mechanical properties: W, Mo, Ir, Ru/Rh
4) Overall best primary element costing material: Ir (best for oxidation, thermal conductivity, and alpha range).

It is worth noting that tungsten and molybdenum must be alloyed with rhenium or other elements (Hf, Zr, C), and ruthenium and rhodium likely need alloying for improved mechanical properties. Optimal alloys for coating are application-specific.

1.1.1 Thermophysical and Thermomechanical Properties of Reactive/Refractory and Precious Metal Group Metals

Selected thermophysical properties of candidate coating elements are provided in Table 1, including melting point (MP), density, thermal conductivity (k_{th}), and the range of 5.6 MeV alpha particles in the metal. Transitional metallic elements in periods 4, 5, and 6 of the periodic table, Groups 3 through 10, are included. The red-colored cells indicate primary elements not suitable for structural use; La and Mn have relatively low melting points and poor thermal conductivity, while Tc is a radioactive artificial element. The Group 3 elements have lower melting temperatures in their respective periods, as well as the lowest densities and generally low thermal conductivity. The light brown- and orange-colored cells indicate elements with lower melting points than other elements in their respective periods, and the green-colored cells indicate metals for potential application subject to temperature and other constraints. The dark green-colored cells show the three best elements for high-temperature applications: W, Mo, and Ir. These elements would most likely be alloyed for improved strength and creep resistance at high temperatures. Mo and W are typically alloyed with Re and fine particles of HfC for improved high-temperature strength and creep resistance, while Ir has been alloyed with W.

Table 1 Thermophysical Properties of Transition Metals of Periods 4, 5, and 6 in Groups 3 through 10 in the Periodic Table

Group	3	4	5	6	7	8	9	10
Element	Sc	Ti	V	Cr	Mn	Fe	Co	Ni
	1539	1667	1890	1875	1244	1535	1495	1455
MP, °C	2.985	4.54	6.11	7.14	7.43	7.874	8.90	8.908
	15.7	22.4	30.7	96.5	7.68	86.5	105	94.1
Density,	15.8	21.9	30.7	93.9	7.83	80.4	100	90.9
g/cm^3 at	-	20.7	31.0	92	-	72.0	89	82.7
20°C	31.7	21.2	16.3	14.1	13.9	13.2	12.0	12.0
	Y	Zr	Nb	Mo	Tc	Ru	Rh	Pd
k_{th}, W/m-	1530	1850	2468	2610	2200	2282	1960	1552
K, at 0°C,	4.5	6.55	8.57	10.22	11.5	12.37	12.39	11.99
20°C,	17,0	23.2	53.3	130.0	50.9	117.0	151.0	71.6
100°C	17.2	22.7	53.7	138.0	50.6	117.0	150.0	71.8
	17.7	21.8	54.8	135.0	50.1	115.0	147.0	73.0
Alpha	29.2	30.3	15.7	13.4	12.0	11.3	11.4	12.0
range,	La	Hf	Ta	W	Re	Os	Ir	Pt
microns	920	2227	2996	3410	3186	3045	2443	1769
	6.17	13.30	16.65	19.30	21.0	22.59	22.56	21.45
	15.8	23.3	57.4	177.0	48.6	88.0	148.0	71.7
	-	23.0	57.5	173.0	48.0	87.6	147.0	71.6
	-	22.4	57.7	163.0	46.6	87.0	145.0	71.7
	26.6	14.3	11.3	9.8	9.1	8.5	8.6	9.1

The melting points and densities are taken from the *Metals Handbook Desk Edition*, Second Edition, J.R. Davis, Editor, p 629–633 (ASM).

Table 2 shows the thermal conductivities of the same elements provided in Table 1, but at higher temperatures of 1,000°C, 1,300°C, and 1,500°C. The dashed entries (-) indicate no data measured, or that the temperature is above the melting point.

Table 2 Melting Points and Thermal Conductivities (at 0°C, 20°C, 100°C, 1,000°C, 1,300°C, 1,500°C) of Transition Metals of Periods 4, 5, and 6 in Groups 3 through 10 in the Periodic Table

Group	3	4	5	6	7	8	9	10
Element	Sc	Ti	V	Cr	Mn	Fe	Co	Ni
	1539	1667	1890	1875	1244	1535	1495	1455
MP, °C	15.7	22.4	30.7	96.5	7.68	86.5	105	94.1
	15.8	21.9	30.7	93.9	7.83	80.4	100	90.9
k_{th},		20.7	31.0	92.0	-	72.0	89	82.7
W/m-K,	-	22.5	41.7	61.9	-	29.6	48.2	77.7
at 0°C	-	25.1	45.5	56.1	-	32.7	42.8	84.0 est
20°C	-	-	48.1	-	-	34.3	43.1	-
100°C	Y	Zr	Nb	Mo	Tc	Ru	Rh	Pd

Group	3	4	5	6	7	8	9	10
1000°C	1530	1850	2468	2610	2200	2282	1960	1552
1300°C	17,0	23.2	53.3	130.0	50.9	117.0	151.0	71.6
1500°C	17.2	22.7	53.7	138.0	50.6	117.0	150.0	71.8
	17.7	21.8	54.8	135.0	50.1	115.0	147.0	73.0
	-	26.7	68.6	108.0	-	92.8	115.0	104.0
	-	29.5	73.2	96.6	-	88.5	110.0	111.0
	-	31.2	76.1	93.3	-	86.2	110.0	115.0
	La	Hf	Ta	W	Re	Os	Ir	Pt
	920	2227	2996	3410	3186	3045	2443	1769
		23.3	57.4	177.0	48.6	88.0	148.0	71.7
		23.0	57.5	173.0	48.0	87.6	147.0	71.6
	14.5	22.4	57.7	163.0	46.6	87.0	145.0	71.7
	-	20.9	61.3	112.0	46.2	86.9	118.0	84.2
	-	21.5	62.5	106.0	48.3	86.9	110.0	91.3
	-	22.0	63.3	103.0	49.8	86.9	-	95.7

Based on this data, we can make several observations to prioritize candidate coating materials. La and Tc can be excluded as previously mentioned, while Sc and Y are unlikely, but interesting light elements. Sc and Y have higher melting points than Mn, Co, and Ni, and are comparable to Fe and Pd. Zr and Hf (and Y) readily oxidize. Mn has both a low melting point and low thermal conductivity that is not suitable as a main alloy element but is a minor alloy element for stainless steels.

In terms of acceptance, the following observations were made:

- Ranked by melting point: W, Re, Os, Ta, Mo, Nb, Ir
- Ranked by k_{th}: W, Rh, Ir, Mo, Ru
- Ranked by least alpha range (or best stopping power): Os, Ir, Pt, Re, W, Ta, Ru, Rh, Pd
- Ranked by elastic modulus (stiffness): Os, Ir, Re, Ru, W, Mo
- Ranked by tensile strength: Os, Ir, W, Rh, Mo, Ru (note that W and Mo can be solid-solution strengthened with Re and dispersion strengthened with HfC, while Ir and Rh can be strengthened with Ru).
- Overall best primary element: Ir (best for oxidation resistance, thermal conductivity, and alpha range).

Ir is compatible with Mo and may be alloyed with Mo or W for improved properties (Morris 1978).

Thermal conductivities and thermomechanical properties are discussed in the following sections. Optimal alloys are application-specific, and matching coating elements to specific use cases is an area for further research.

1.1.2 Thermal Conductivity

The thermal conductivities of the periods 4, 5, and 6 transition metals in Groups 3–10 of the periodic table are given in Figure 1, Figure 2, and Figure 3, for Periods 4, 5, and 6, respectively. The data are taken from a comprehensive review of the thermal conductivity of the elements by Yo et al. (1974).

Sc and Mn have poor thermal conductivities, although not much information is available for Sc due to its rarity. The Group 4 elements (Ti, Zr, and Hf, all hexagonal close-packed metals) show very low thermal conductivity that increases slightly with temperature. The Group 5 elements (V, Nb, and Ta) have moderate thermal conductivities; the conductivities of V and Nb increase more strongly with temperature than that of Ta, although the conductivities of Nb and Ta are similar. Groups 6 and 8 elements show a decrease in thermal conductivity with temperature, although the conductivity of Os is relatively flat vs. temperature.

Group 7 metals have low thermal conductivity, with Mn having the poorest and Tc and Re having similar thermal conductivity. Group 9 metals (Co, Rh, and Ir) have relatively high thermal conductivity at room temperature but show decreasing conductivity with increasing temperature. Interestingly, Co shows lower conductivity than Cr, but for the corresponding heavier elements, the trend changes, with Rh having a greater conductivity than Mo, and Ir conductivity exceeding that of W over most of the temperature range for which there is data for Ir.

The Group 10 metal considered (Ni) shows a unique trend in which thermal conductivity decreases with temperature, but then turns around (at about 400°C) and increases with temperature, while Pd and Pt show an increasing trend over their temperature ranges.

W has the highest thermal conductivity at room temperature but then falls below that of Rh and Ir, which have similar thermal conductivities, which appear to converge at 1,300°C. W has the highest melting point making it the only metal capable of performing at temperatures above Re and Os. For practical structural purposes, one would not use a structural material beyond about 0.8 homologous temperature, but at low stress, or more likely at lower values of 0.5 to 0.7, where creep would be a concern for service life. The homologous temperature of a crystalline material is defined as T/T_m, where T is temperature and T_m is the melting (solidus) temperature on an absolute scale, usually in Kelvin.

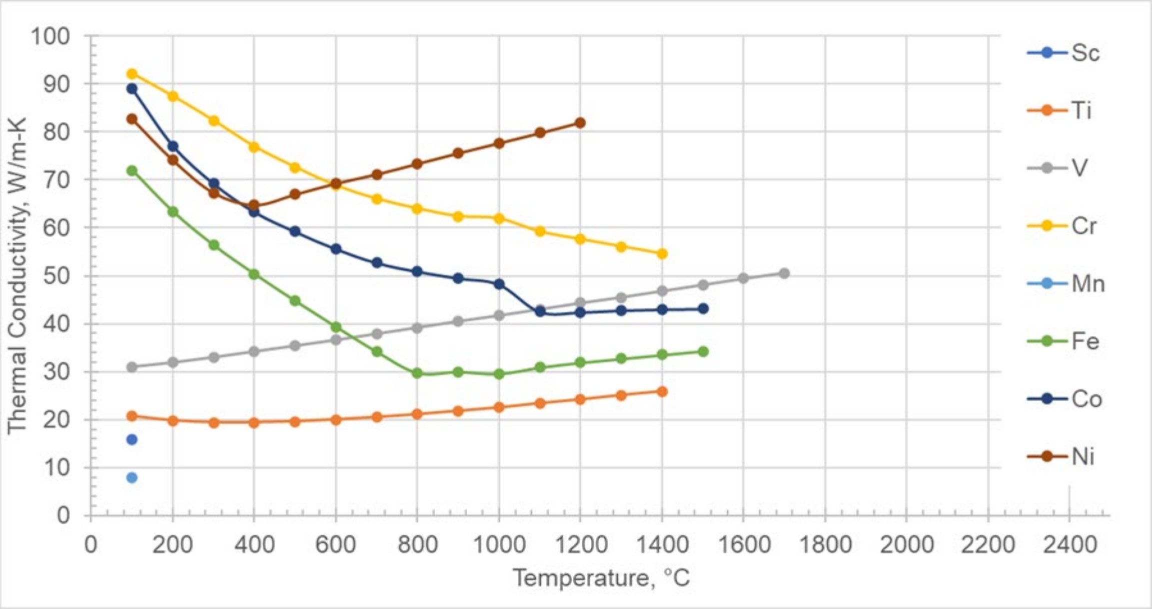

Figure 1 Thermal Conductivities as Functions of Temperature for Transition Metals in Period 4, Groups 3–10: Sc, Ti, V, Cr, Mn, Fe, Co, Ni

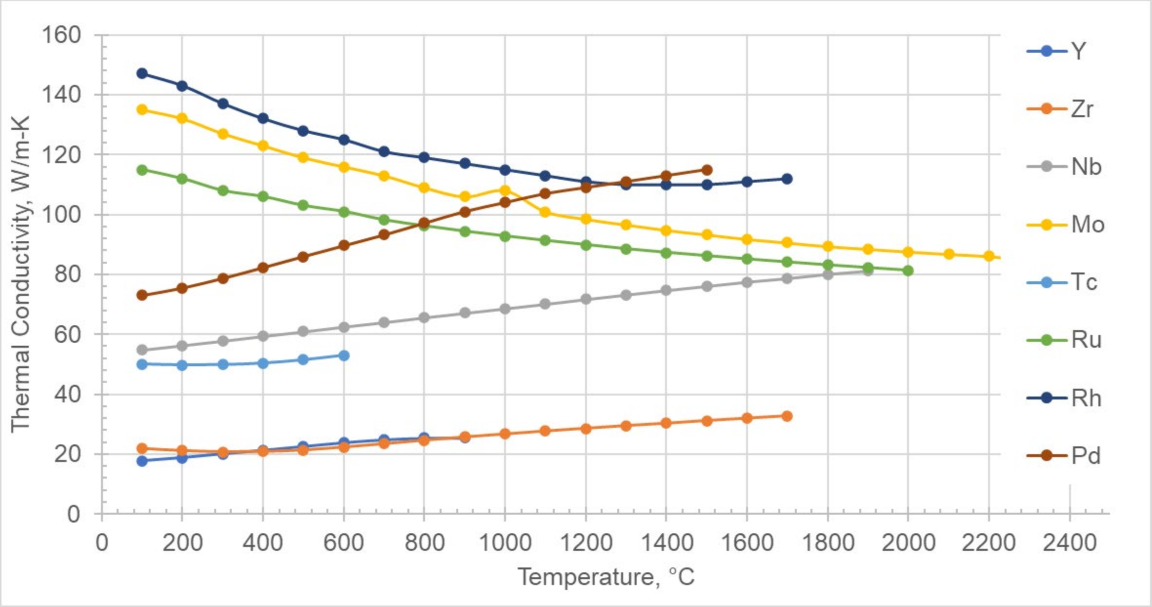

Figure 2 Thermal Conductivities as Functions of Temperature for Transition Metals in Period 5, Groups 3–10: Y, Zr, Nb, Mo, Tc, Ru, Rh, Pd

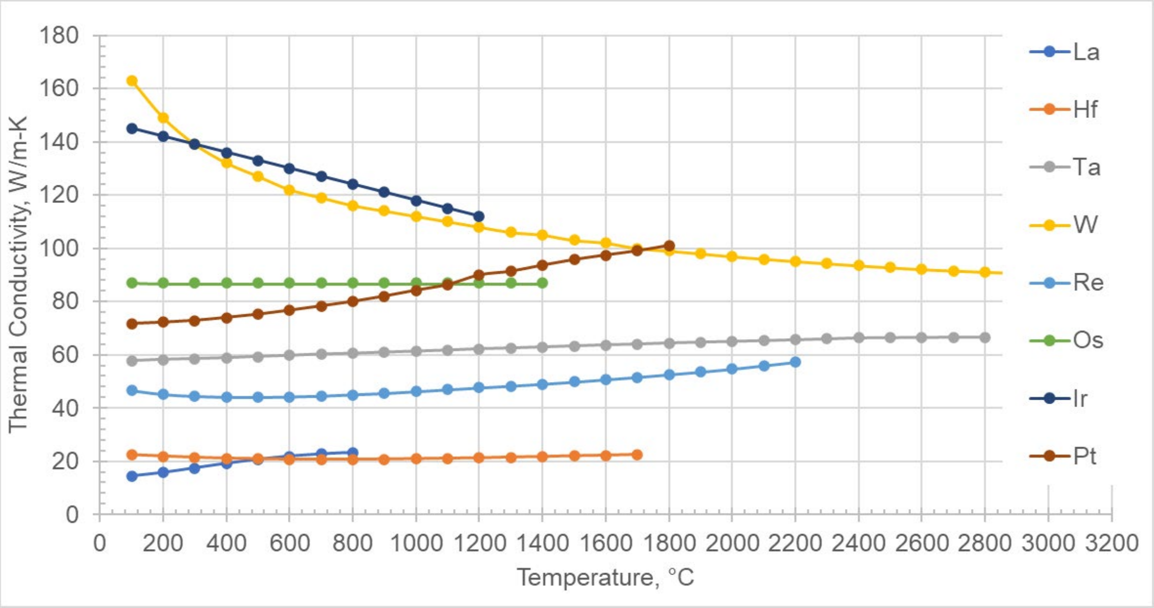

Figure 3 Thermal Conductivities as Functions of Temperature for Transition Metals in Period 6, Groups 3–10: La, Hf, Ta, W, Re, Os, Ir, Pt

1.1.3 Thermomechanical Properties

The room temperature mechanical properties are provided in Table 3 and Table 4 for the precious metal group elements and Period 5 and 6 reactive and refractory metals, respectively. The elastic moduli are compared in Table 5.

Table 3 Room Temperature Mechanical Properties of Precious Metal Group Elements (Lyon 2010)

Element	Elastic modulus, GPA	YS, MPa	UTS, MPa	Elongation, %
Ru	420	370	430	3
Rh	315	80	700	15
Pd	115	50	190	40
Os	555	brittle	brittle	brittle
Ir	515	235	1,100 (?)	10
Pt	170	45	150	40
Pt-40% Rh	-	95	510	30

Table 4 Room Temperature Mechanical Properties of Refractory and Reactive Elements (Unverified, for information only) (Tietz and Wilson 1961)

Element	Elastic modulus, GPA	YS, MPa	UTS, MPa	Elongation, %
Nb	99, 103	207		5–30
Mo	333	420	509	-
Ta	186	100	170–450	10–30
W	405–407	400, 750	980	-
Re	470	290	1070	-

Table 5 Room Temperature Elastic Moduli and Poisson's Ratio of Period 5 and 6 Transition Metals (Darling 1966)

Element	Crystal Structure	E GPa	G GPa	K GPa	v	E/2G-1
Zr	HCP	94.7	35.7	88.6	0.33	0.325
Nb	BCC	102.9	36.2	171.6	0.38	0.421
Mo	BCC	336.9	118.4	271.8	0.30	0.422
Tc	HCP	388.3	155.3	277.7	0.26	0.250
Ru	HCP	417.5	167.0	283.5	0.25	0.250
Rh	FCC	375.1	148.5	271.9	0.26	0.263
Pd	FCC	124.6	44.8	185.3	0.39	0.392
Hf	HCP	136.9	52.4	108.3	0.30	0.306
Ta	BCC	182.7	68.0	204.4	0.35	0.344
W	BCC	384.5	147.0	309.3	0.29	0.308
Re	HCP	458.2	174.8	330.1	0.26	0.311
Os	HCP	543.7	213.6	368.9	0.25	0.273
Ir	fcc	522.6	207.8	367.0	0.26	0.258
Pt	fcc	168.9	60.4	272.7	0.39	0.399

The strongest/stiffest metal in Period 5 is Ru, with Os the strongest/stiffest in Period 6. These metals are consequently the most brittle. Iridium is the second strongest metal in Period 6, while Rh is the second, excluding Tc. The properties may vary considerably among similar elements or alloys from different sources. For example, Ru is reported to have an elastic modulus of 447 GPa, shear modulus of 173 GPa, bulk modulus of 220 GPa, UTS 370 MPa (materials-properties.org).

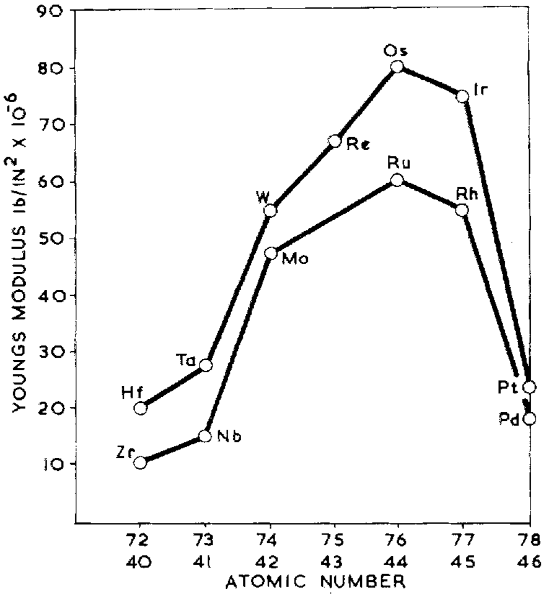

Figure 4 Room Temperature Elastic (Young's) Moduli of Period 5 and Period 6 Transition Metals

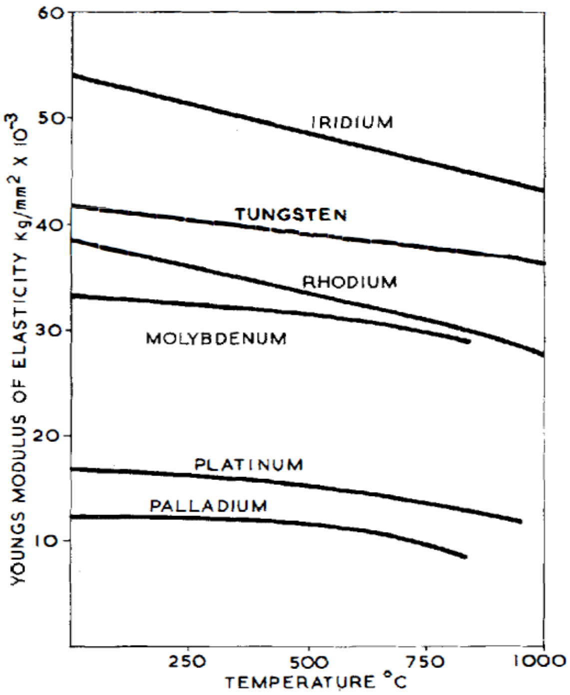

Figure 5 Elastic (Young's) Moduli of Period 5 and Period 6 Transition Metals as Functions of Temperature from 0°C to 1,000°C

Strength can be increased for each element through solid solution strengthening, e.g., the addition of Re to Mo or W, or through dispersed strengthening (precipitation hardening) of carbides, e.g., HfC. Pt can be strengthened with additions of Rh and W, and Ir is strengthened with additions of W and small amounts (~ 60 ppm) of Th and/or Ce (Axler and Eash 1987; Schneibel et al. 2017; Song et al. 2015) in Ir-alloy DOP-26.

Ir and Pt have the greatest oxidation resistance but lack strength at high temperatures, while W and Mo, and particularly their alloys, have high strength and creep resistance at very high temperatures, e.g., > 1,300°C, but they lack oxidation resistance. An appropriate application may be to coat a ceramic oxide, e.g., PuO_2, with a layer of Ir or Pt (or alloy) and then apply a mechanical substrate consisting of an appropriate Mo or W alloy. This approach is discussed in the applications section.

1.1.4 Alpha Range in Metals

The range in air for a 5.6 MeV alpha particle from ^{238}Pu is calculated to be 41.48 mm, based on an air density of 0.00129 kg/m^3 and air molecular mass of 14.74 g/mol.

Table 6 Range of 5.6 MeV Alpha Particles in Periods 4, 5, and 6 Transition Metals

Element	Z	Range in air (mm)	Element At. Mass	Element Density	Range (mm)	Range (microns)	NIST CSDA	Difference, Fraction (Tsoulf -NIST)	
Sc	21	41.47882	45.956	2.98	0.0317	31.65			
Ti	22	41.47882	47.867	4.54	0.0212	21.24	18.07	3.17	0.175
V	23	41.47882	50.942	6.11	0.0163	16.28			
Cr	24	41.47882	51.996	7.14	0.0141	14.08			
Mn	25	41.47882	54.938	7.43	0.0139	13.90			
Fe	26	41.47882	55.845	7.87	0.0132	13.23	11.54	1.69	0.147
Co	27	41.47882	58.933	8.90	0.0120	12.02			
Ni	28	41.47882	58.693	8.91	0.0120	11.99			
Y	39	41.47882	88.906	4.50	0.0292	29.20			
Zr	40	41.47882	91.224	6.55	0.0203	20.32			
Nb	41	41.47882	92.906	8.57	0.0157	15.68			
Mo	42	41.47882	95.95	10.22	0.0134	13.36	11.47	1.89	0.164
Tc	43	41.47882	98	11.50	0.0120	12.00			
Ru	44	41.47882	101.07	12.37	0.0113	11.33			
Rh	45	41.47882	102.906	12.39	0.0114	11.41			
Pd	46	41.47882	106.42	11.99	0.0120	11.99			
La	57	41.47882	138.905	6.17	0.0266	26.62			
Hf	72	41.47882	178.49	13.00	0.0143	14.32			
Ta	73	41.47882	180.948	16.65	0.0113	11.26			
W	74	41.47882	183.94	19.30	0.0098	9.79	10.17	−0.37	−0.037
Re	75	41.47882	186.207	21.00	0.0091	9.06			

Os	76	41.47882	190.23	22.59	0.0085	8.51			
Ir	77	41.47882	192.217	22.56	0.0086	8.56			
Pt	78	41.47882	195.084	21.45	0.0091	9.08	9.52	−0.44	−0.047

The ranges of alpha particles in Periods 4 and 5 seem to be conservatively estimated compared to current National Institute for Standards and Technology (NIST) data; however, the ranges may not be conservatively estimated for Period 6 elements. In all three periods, the alpha range decreases with increasing Z, which is consistent with the dominance of the electron-stopping power.

The range of an alpha particle in the air is given by the equation (Tsoulfanidis and Landsberger 1995):

$$R_{air}\ (mm) = (0.05\,T + 2.85)T^{3/2}\ (MeV),\ \ 4\ \le T < 15\ MeV\ ,$$

where T is the kinetic energy of the alpha particle.

The range of alpha particles R_m in a different material based on the Bragg-Kleeman rule (Tsoulfanidis and Landsberger 1995) is as follows:

$\frac{R_2}{R_1} = \frac{\rho_1}{\rho_2}\sqrt{\frac{A_2}{A_1}}$, let $R_2 = R_m$ and $R_1 = R_{air}$ => $R_m = R_{air}\,\frac{\rho_{air}}{\rho_m}\sqrt{\frac{A_m}{A_{air}}}$

NIST data on continuous slowing down approximation (CSDA) may be found online at NIST's website: https://physics.nist.gov/cgi-bin/Star/ap_table.pl.

In terms of stopping power for alpha particles, the following elements are ranked from most effective (greatest stopping power or shortest range) to least effective: Os, Ir, Pt, Re, W, Ta, Ru, Rh, Pd(Ni). The most oxidation-resistant elements, Ir and Pt, are also the most effective for stopping alpha particles after Os, which has poorer oxidation resistance.

1.1.5 Cost of Precious Metal Group and Reactive/Refractory Metals

Precious metal group elements are typically used in very thin (microns) layers due to their high cost. Reactive and refractory metals are less expensive, but they are used for special applications requiring high temperatures. The prices of reactive/refractory and precious metal group elements are subject to considerable market volatility due to the availability (often from sensitive nations and rarity) and demand volatility. As of August 2024, the price of Rh, which was the highest of the precious metal group, fell below that of Ir.

Some representative prices (for information only, as of August 2024) are as follows:

Osmium

- $41,351.00 per troy oz ($1,329,464/kg)
- >$64,000.00 per troy oz (>$2,057,645/kg)

Rhodium

- ~$4700 per troy oz ($151,092/kg)

Iridium

- ~$4700 per troy oz ($151,092/kg)

Palladium

- ~$947.00 per troy oz ($30,443/kg)

Gold

- $1,774.70 per troy oz. ($57,057/kg)

Platinum

- ~$948.00 per troy oz ($30,475/kg)

Ruthenium

- ~$400.00 per troy oz. ($12,859/kg)

Tungsten

- ~$45,000 to 50,000 per metric ton (~$45–50/kg)

Cobalt

- $33,000 per metric ton ($33/kg)

Molybdenum

- $26,000 per metric ton ($26/kg)

Nickel

- $22,134.78 per metric ton ($22/kg)

Copper

- $8,243.16 per metric ton ($8/kg)

Iron

- $104.52 per metric ton ($0.10/kg)

Osmium is the most expensive, followed by Rh and Ir. Rhodium is much more expensive than iridium, but prices of Rh fell considerably from 2021 through 2023, and now Rh is less expensive than Ir, although the price of both seems to be converging. Prices are subject to change (during some periods the change can be dramatic depending on supply and demand) and are provided for general information only.

1.1.6 Applications of Precious Metal-Coated Microspheres

RPS are a mature technology in the United States. Alloys of Ir and Pt have been developed for this application, using fuels such as $^{238}PuO_2$. Encapsulating microspheres of PuO_2 requires at least 10 microns, and preferably 15 microns, of Ir or Pt to stop all alpha particles from escaping the ceramic microsphere. If additional thickness is needed, Mo-alloy may be overlaid on the Ir base.

For nuclear reactor systems, a Mo-Re-alloy may be best suited in terms of strength at high temperatures, high thermal conductivity, relatively low density compared to heavier metals (Ta, W, Re, and Ir), and low cost, compared to the precious metal group elements. Luo et al. (1994) provided a review of the status of Mo 5 wt% Re 0.5 wt% HfC as of 1994, which is a type of Mo-RHC, which was still in the research stage at the time, and currently, there is no UNS number of ASME code or ASTM standard for the alloy or its derivatives. Obtaining an ASME code case and UNS number requires the production of several heats of the material, usually at least three heats in commercial quantities fabricated in the appropriate form. While there are several Mo alloys manufactured in commercial quantities, Mo-RHC is so unique (can be costly) that it is not a commercial grade. Yet, of the potential alloys for a high-temperature nuclear reactor, it would be advantageous to use a Mo-alloy over W and Ta alloys (Klopp 1985) due to its lower neutron absorption (capture) compared to W or Ta. Some of the precious metal groups, namely Ru, Rh, Ir, and Pt, may provide a benefit to a Mo-Re-HfC-alloy system, e.g., as a protective surface coating or alloying agent, but this must be explored, and little has been done since 1994, or even since 1984.

For both applications in RPS or high-temperature nuclear reactors, the issue of compatibility or stability of layered precious metal groups and reactive/refractory alloys must be considered. In some cases, e.g., Ir, the compatibility of metal oxides has been assessed (Axler and Eash 1987). Furthermore, the compatibility of Ir and Mo has been addressed by JF Morris in U.S. Patent 4111718 (Morris 1978).

In the summary of that invention, the inventor notes, “Sensors composed of molybdenum, iridium, and alloys containing only these two metals provide advantages over prior art thermocouples as a result of the physical and chemical compatibility of molybdenum and iridium at high temperatures and in vacuum systems.” Furthermore, the inventor states, “The compatibility of molybdenum and iridium at elevated temperatures reduces the problem of preferential evaporation in the molybdenum, iridium thermocouple sensor to provide a more stable emf-temperature relationship. The vapor pressure and physical and chemical compatibility of molybdenum, iridium, and alloys containing only these two metals reduce thermocouple hot-junction failures and allow such sensors to be employed in high-temperature and vacuum systems without the necessity of metallic sheaths and ceramic insulation at operating temperatures up to about 2,450°C. The advantages of the present invention are further enhanced over tungsten-rhenium and tantalum-rhenium combinations in that the present invention does not contain rhenium which is often very expensive and sometimes unavailable.” Since the patent was awarded, rhenium is more readily available, and its relative cost has been reduced. It should be noted that Ir would have no strength at ~2,450°C, and Mo would have little strength. Such a high temperature would require a W alloy, carbide, and perhaps graphite structure, or some combination. Further research is needed to identify the appropriate alloy for the desired temperature and coolant environment.

Coating compatible with other fuel materials, e.g., UMo, UZr, UC, or UN, must be further researched; UN is preferred for the higher thermal conductivity and low fission gas release; however, at very high temperature and with irradiation, free nitrogen becomes available and would chemically interact with the cladding. Rhenium (Re) has been proposed as a coating, but a precious metal group may also be applied, possibly to the ceramic fuel particles. The coating (Ir, Pt, and Rh) should be as thin as possible, and also be compatible with the cladding material, which would likely be a Mo-Re alloy for minimal parasitic neutron absorption (Klopp 1985).

Garcia and Goto (2003) suggest Ir is compatible with graphite, and possibly carbides: " [chemical vapor deposition (CVD)] of iridium is of interest to prepare oxidation-resistant protective coatings on structural graphite for temperatures above 1773K because of the compatibility of iridium with carbon materials (i.e., no carbide formation)."

For catalysis, and particularly selective catalysis, it may be desirable to have different layers, perhaps porous layers, of precious metal group elements on the surface of an oxide microsphere. The microsphere could be alumina (Al_2O_3), yttria (Y_2O_3), ceria (CeO_2), zirconia (ZrO_2), or some other rare earth oxide.

Vargas Garcia and Goto also point to interests in depositing platinum, rhodium, and palladium on surfaces for catalytic function, e.g., "Platinum catalysts prepared in a fluidized-bed CVD reactor are promising for hydrocarbon conversion applications."

More pointed, Shapley et al. (2002) show an interest in "bimetallic clusters of Ir and Mo deposited on 'fumed alumina'."

2.0 Experimental Methods

The following were purchased from Milipore Sigma and used without further purification…" then break out the rest into bullets so it is easier to read:

- Platinum acetylacetonate (Pt acac, CAS: 15170-57-7, 99.8%)
- Platinum (II) chloride ($PtCl_2$, CAS: 10025-65-7, 98%)
- Palladium (II) chloride ($PdCl_2$, CAS: 7647-10-1, 99%)
- Iridium (III) chloride ($IrCl_3$, CAS:10025-83-9, 99.8%)
- Tungsten hexacarbonyl ($W(CO)_6$, CAS: 14040-11-0, 97%)
- Rhenium (III) chloride ($ReCl_3$, CAS: 13569-63-6, 99%+)
- Rhodium acetylacetonate (Rh acac, CAS: 14284-92-5, 97%)
- Ruthenium (III) chloride ($RuCl_3$, CAS: 14898-67-0, 99.9%+)
- Tantalum (V) chloride ($TaCl_5$, CAS: 7721-01-9, 99.8%+)
- Molybdenum (V) chloride ($MoCl_4$, CAS: 10241-05-1, 95%)
- Titanium (IV) chloride ($TiCl_4$, CAS: 7550-45-0/ 99%+)
- Ethylene glycol (EG, CAS: 107-21-1, 99%+)
- Choline chloride (CAS: 67-48-1, 99%+)
- (3-aminopropyl)trimethoxysilane (APTMS, CAS: 13822-56-5, 97%)
- Potassium hydroxide (KOH, CAS: 1310-58-3, 99%+)
- Methanol (MeOH, CAS: 1310-58-3, 99%+) Metallic Coating Methods

The coating is applied in three steps:

1) A surface preparation step resulting in N-CeO_2
2) A functionalization step resulting in CeO_2-NH_2
3) An electroless plating step resulting in CeO_2 microspheres coated with metal.

1) For the first step, a sample of the ceria microspheres, typically 50–150 mg, was added to a 20 mL glass vial with a small, glass-coated stir bar that had previously been acid-leached. One mL of ammonium hydroxide (14.8 M) and 5 mL deionized water were added to the vial. The vial was then capped, and the solution was stirred at 100 rpm at room temperature for 24 hours. The solution was decanted off the microspheres and added to a waste container. A squeeze bottle was used to rinse the entire inner surface of the vial with DI water, using approximately 5 mL of water. The microspheres were manually swirled in the water in the vial for approximately 30 seconds, then the rinse water was decanted, and also added to the waste container. This process was repeated twice, for a total of three rinses. At any point, if any of the microspheres were floating on the surface of the liquid, the vial was capped and centrifuged at 4,400 rpm for 2 minutes before decanting. The vial was held at an angle and tapped on a firm surface (e.g., the bottom of a fume hood) to spread the microspheres across the bottom of the vial, then the entire vial was placed into a forced air convection oven at 105°C. The microspheres were dried until

they flowed freely across the bottom of the vial, typically 30–60 minutes. The microspheres were stored in the vial, capped, until use.

2) For the second step, a sample of the N-CeO_2 microspheres, typically 5–80 mg, was added to a 20 mL glass LSC vial with a small, glass-coated stir bar that had previously been acid-leached. Ten mL of methanol and 0.5 uL of (3-aminopropyl) trimethoxysilane (APTMS) were added to the vial. The vial was then capped, and the solution was stirred at 400 rpm at room temperature for 30 minutes. The solution was decanted off the microspheres and added to a waste container. The vial was held at an angle and tapped on a firm surface (e.g., the bottom of a fume hood) to spread the microspheres across the bottom of the vial, then left uncapped and allowed to air dry until the microspheres flowed freely across the bottom of the vial, typically 30–60 minutes. The microspheres were then either used immediately or stored in the vial, capped, until use.

3) For the third step, one bead of KOH (typically 0.1 g) was added to 20 mL of ethylene glycol in a 20 mL glass LSC vial and sonicated until dissolved, typically 20–30 minutes. The prepared solution was stored in a laboratory refrigerator until used. A sample of the CeO_2-NH_2 microspheres, typically 2–20 mg, was added to a 20 mL LSC vial with a small, glass-coated stir bar that had previously been acid-leached. Twenty-five uL of 1-butyl-3-methylimidazolium tetrafluoroborate (BMIM-BF_4) and a metal precursor, typically 3–10 mg, were added to the vial with 10 mL of the KOH/ethylene glycol mixture. A list of the metal precursors used can be found in Table 7. The vial was then capped, and the solution was stirred at 400 rpm on a hot plate set to 195°C for some time, typically 6 hours. The heating function on the hot plate was turned off, but the stirring was left on while the vial cooled. Once the vial was cool enough to handle, typically 30 minutes, the vial was centrifuged at 4,400 rpm for 2 minutes. The solution was decanted off the microspheres and added to a waste container.

Table 7 Metal Precursors and Summary Results of the Coating Process

Metal Precursor	Alloys attempted
Platinum acetylacetonate (Pt Acac)	
Platinum (II) chloride ($PtCl_2$)	Pt/Rh
Palladium (II) chloride ($PdCl_2$)	
Iridium (III) chloride ($IrCl_3$)	Ir/W
Tungsten hexacarbonyl ($W(CO)_6$)	Ir/W, Re/W
Rhenium (III) chloride ($ReCl_3$)	Re/W
Rhodium acetylacetonate (Rh Acac)	Pt/Rh
Ruthenium (III) chloride ($RuCl_3$)	
Tantalum (V) chloride ($TaCl_5$)	
Molybdenum (IV) chloride ($MoCl_4$)	Mo/Re
Titanium (IV) chloride ($TiCl_4$) (in Ethaline solvent)	

Two other types of coating were attempted: alloy coatings (two metals applied simultaneously) and double coatings (two metals applied sequentially). For alloy coatings, two metal salts were added to the vial. A list of the alloys attempted can be found in Table 7. For double coatings, the microspheres were heat treated at 250°C for 72 hours in a vacuum furnace (rough pump). Then, the electroless plating step was repeated with a second metal. The double coatings attempted were platinum over iridium and palladium over iridium.

2.1 Cerium Leach Testing

As iridium coating was selected based on positive coating results and the guidance of the materials selection team, both iridium-coated and coated microspheres were heated in a furnace and then exposed to methanol (dissolves CeO_2) for 72 hours. In such a way any holes in the iridium coating would correspond to increased cerium concentration when the leachate was processed by an external inductively coupled mass spectrometry (ICPMS) team.

Both pre-coated cerium microspheres and powders that had been previously heated to 1,600°C were used to benchmark the test. Iridium-coated spheres were first heated to 400°C in air for 1 hour to drive off any water and organics then heated to 1,000°C for 2 hours in air. The furnace schedule was thus:

1) Ramp up 20°C–400°C at 10°C/min (38 minutes)
2) Hold at 400°C for 60 minutes
3) Ramp up 400°C–1,000°C at 2°C/min (300 minutes)
4) Hold at 1,000°C for 120 minutes
5) Let cool to ambient (about 6 hours).

Samples of the spheres at each process step were then exposed to pure methanol at ambient for 72 hours. The liquids were collected and analyzed for cerium concentration (as well as other contaminants such as iridium). This methodology allowed for the quantitative determination of the leach rate of the spheres and for an objective lens through which to evaluate the protective properties of the metal coating.

2.2 Characterization Equipment

Optical imaging was taken with an OMAX 2400 UV-epi fluoroscope (100 W mid-pressure UV bulb centered at 325 nm, broad emission) and Dinolite 375 nm emitting endoscope (AM4517MT-FUW). All sample stages were mounted with vendor-supplied 4-axis. The images were recorded with vendor-supplied software and converted to bit maps for processing, if available, and the scale bars were burned into the images for direct control of the scale during processing. The images were processed with Image J software v.1.54f.

Scanning electron microscopy (SEM) was performed on a JEOL IT-800 equipped with an Oxford X-Max energy dispersive spectrometer (EDS). Variable accelerating voltages ranging from 5 to 30 kV were used. Scanning transmission electron microscopy (STEM) was done on a JEOL ARM200CF aberration (Cs) corrected microscope operated at 200 kV using a JEOL Centurio EDS detector with a solid collection angle of 0.9 sR.

XPS measurements were performed using a Physical Electronics Quantera SXM Scanning X-ray Microprobe. This system uses a focused monochromatic Al Kα X-ray (1486.7 eV) source for excitation and a spherical section analyzer. The instrument has a 32-element multichannel detection system. The X-ray beam is incident normal to the sample and the photoelectron detector is at 45° off normal. High-energy resolution spectra were collected using a pass-energy of 69.0 eV with a step size of 0.125 eV. For the Ag $3d_{5/2}$ line, these conditions produced a full width at half max (FWHM) of 0.92 eV ± 0.05 eV. The binding energy (BE) scale is calibrated using the Cu $2p_{3/2}$ feature at 932.62 ± 0.05 eV and Au $4f_{7/2}$ at 83.96 ± 0.05 eV. Low energy electrons at ~1 eV, 20μA, and low energy Ar^+ ions were used to minimize sample charging during analysis.

2.3 Methodology of Size Determination

Images were analyzed to determine the diameter of the spheres. First, the size of a pixel in the image needed to be equated to a length. An image taken with the same machine will produce the same scale each time. The length of a pixel may vary based on the magnification factor. This is all handled by setting the scale in ImageJ to each image containing samples. By telling ImageJ some number of k pixels are l μm, we know there are k pixels per l μm, so a sample with a diameter of d pixels is $d * k/l$ μm. Each sample in a photo was measured to a minimum of 20 samples. However, the photos of uncoated cerium oxide before any attempt at electroplating had a minimum of 30. This was an attempt to reduce the magnitude of the margin of error for the “true” diameter.

All data collected with ImageJ was analyzed using Microsoft Excel. The primary derived metrics were the mean diameter, and a 95% confidence interval of the population mean. Data was also analyzed for outliers. If an outlier was found, the analysis to find the mean and 95% confidence interval was conducted with and without the outlier. Outliers were defined as being 1.5 times larger than the third quartile or 1.5 times smaller than the first quartile.

Measuring diameter with photos and ImageJ presents some sources of discrepancies and limitations. Identifying pixels that contain samples is up to the researcher and is limited by image quality. This is mitigated by consistency; the same researcher should measure all the samples for a given experiment. Although not ideal, this will help maintain systemic errors. Another example is the focus and megapixel count of the camera taking the photos to be analyzed. Due to the scale of the samples and the monocular camera lens, not all samples may have the same focus, and some samples may appear ellipsoidal although those samples are spherical. A higher megapixel count allows for more image fidelity.

3.0 Results

Three types of cerium oxide spheres were studied in this work. There were two cerium oxides fired to 650°C and washed by different methods (Katalenich 2017) and one fired to 1600°C. The ceria spheres' surfaces are compared in Figure 8. Figure 8a shows the XPS data for the higher-fired ceria with an inlay micrograph of the white spheres. The spheres seen in Figure 8b were fired at a lower temperature and appear to contain less salt contamination on the surface compared to Figure 8a. The spheres were then coated with an amine layer to continue the coating process.

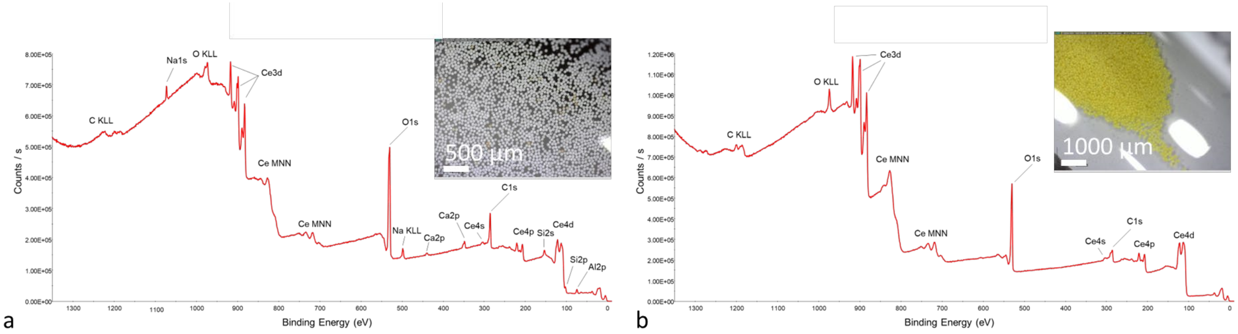

Figure 6 a) An XPS Spectrum Showing the Atomic Constituents of the Surface of the Cerium Microspheres Fired to 1,600°C with an inlay micrograph of the spheres. b) An XPS Spectrum Showing the Atomic Constituents of the Surface of the Cerium Microspheres Fired to 650°C with an Inlay Micrograph of the Spheres.

The XPS data presented in Figure 9 demonstrates the coating procedure. The control data in Figure 9a shows that the background is about ⅒ the magnitude of the data coming from the spheres. The surface of the last remaining ceria is presented in Figure 9b, and shows some small differences when compared to Figure 8b (there was no distinguishable difference in the later coating performance of both types of 650°C fired CeO_2). Amine termination was found to influence the ceria.

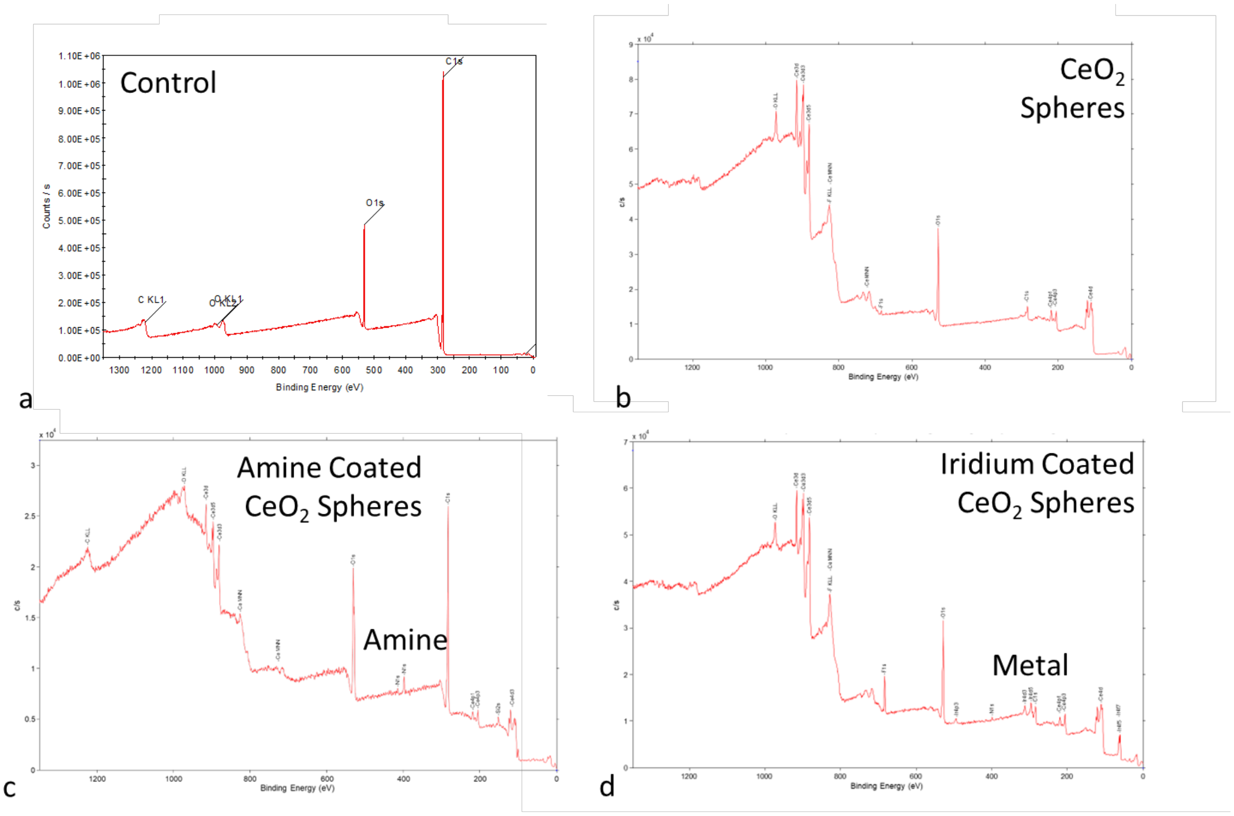

Figure 7 a) An XPS Spectrum Showing the Atomic Constituents of the Control Background Adherent. b) An XPS Spectrum Showing the Atomic Constituents of the Surface of the Cerium Microspheres Fired to 650°C. c) An XPS Spectrum Showing the Atomic Constituents of the Surface of the Amine-Terminated Cerium Microspheres in (b) Showing the Addition of Nitrogen Responses. d) An XPS Spectrum Showing the Atomic Constituents of the Surface of Iridium-Coated Cerium Microspheres with Responses from Iridium Present.

The XPS response of the amine-terminated spheres shows the addition of nitrogen response to the CeO_2 signature, Figure 9c. It was found that the amine termination procedure would dissolve the ceria microspheres after 16–24 hours. As a result of this, the amine termination procedure was shortened to 4 hours, which had no discernible influence on the diameter of the ceria microspheres.

Amine-terminated spheres were then coated in various metals. The XPS spectrum from an iridium-coated sphere is seen in Figure 9d. The presence of iridium is seen in the spectrum along with a decreased presence of carbon and oxygen, suggesting the metallic composition of the coating. The coatings were then analyzed for composition with electron microscopy.

Figure 10, presents the SEM/EDS analysis of the coated spheres. Figure 10a shows a micrograph of the ceria sphere with the pores to the interior of the sphere visible on the surface. Figure 10b shows a ceria sphere after coating with iridium. The diameter has increased, and charge trapping (white signal hue) is seen on the metallic shell as the core-shell nature of these structures lends itself to a natural capacitor. The EDS data presented in Figure 10c shows the cerium signal map confirming that the ceria is still inside the metal shell. The metal signal map also shows that the metal is outside the core by the increase as the edge of the sphere is scanned, Figure 10d. As the coatings appear to be mostly metallic, optical imaging and analysis were used to determine the shell thicknesses.

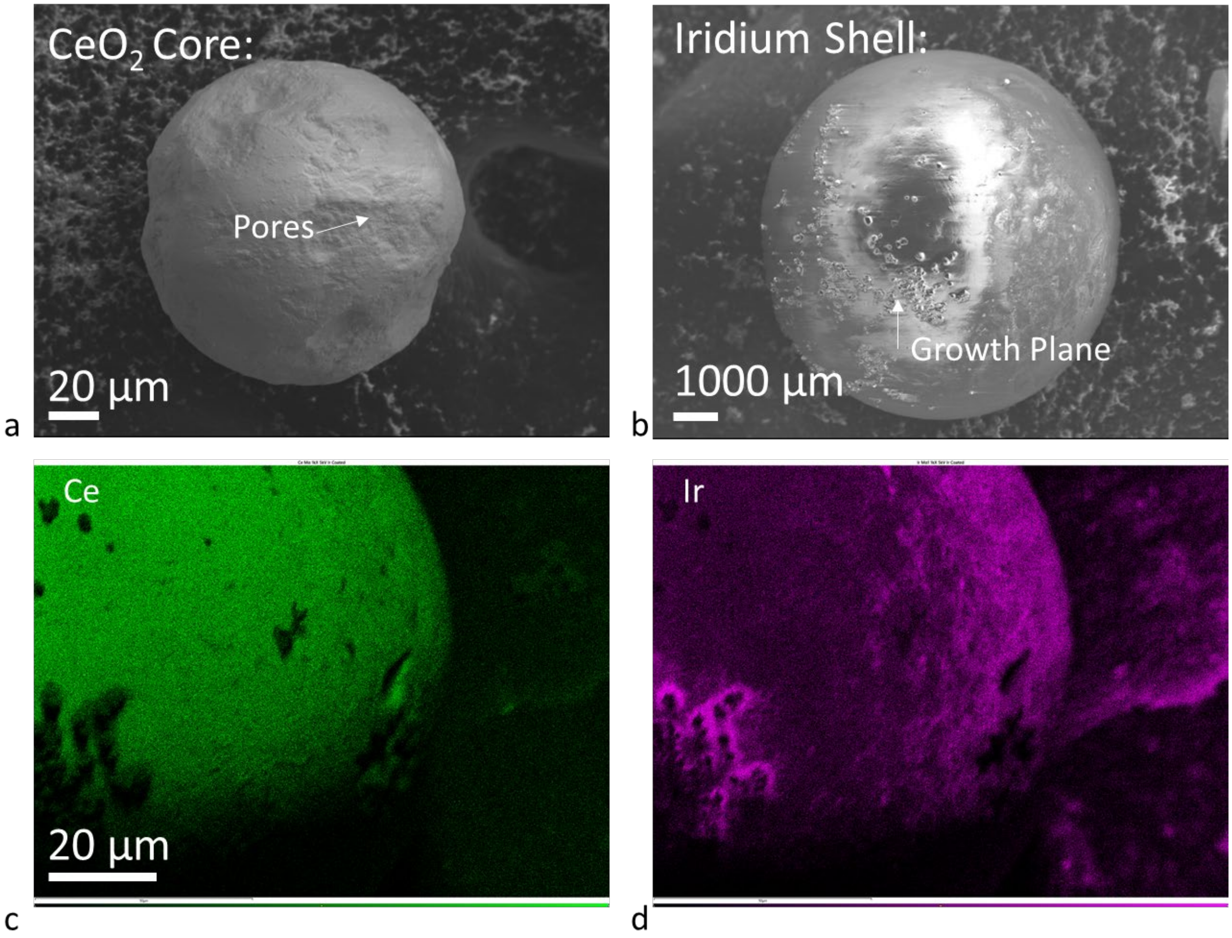

Figure 8 a) SEM Micrograph of an Uncoated Cerium Oxide Microsphere, With a Demarcation of the Pores. b) An SEM Micrograph of an Iridium-Coated Microsphere. c) EDS Map of the Cerium Response from an Iridium-Coated Microsphere. d) EDS Map of the Iridium Response of an Iridium-Coated Microsphere.

A direct size comparison is presented in the image shown in Figure 11a. The darker metal-coated spheres are significantly larger than the cerium cores (light yellow-green spheres). After coating, large batches such as the one shown in Figure 10b could be used to gain a statistical understanding of the sphere diameters and thus shell thickness. Optical imaging also verified that the spheres were completely covered by looking for light transmission through the metal coatings (Figure 10c and d). Ultraviolet imaging was used as well to evaluate that metal reduction was complete by evaluating the spheres for surface salt and aromatic carbon content, Figure 10e. Last, a final check was completed with red to near-infrared imaging of the spheres to evaluate the presence of oxide formation in the coatings, as oxides tend to fluoresce and reflect these wavelengths. The metal sphere data was then compiled for comparison between metals and alloys.

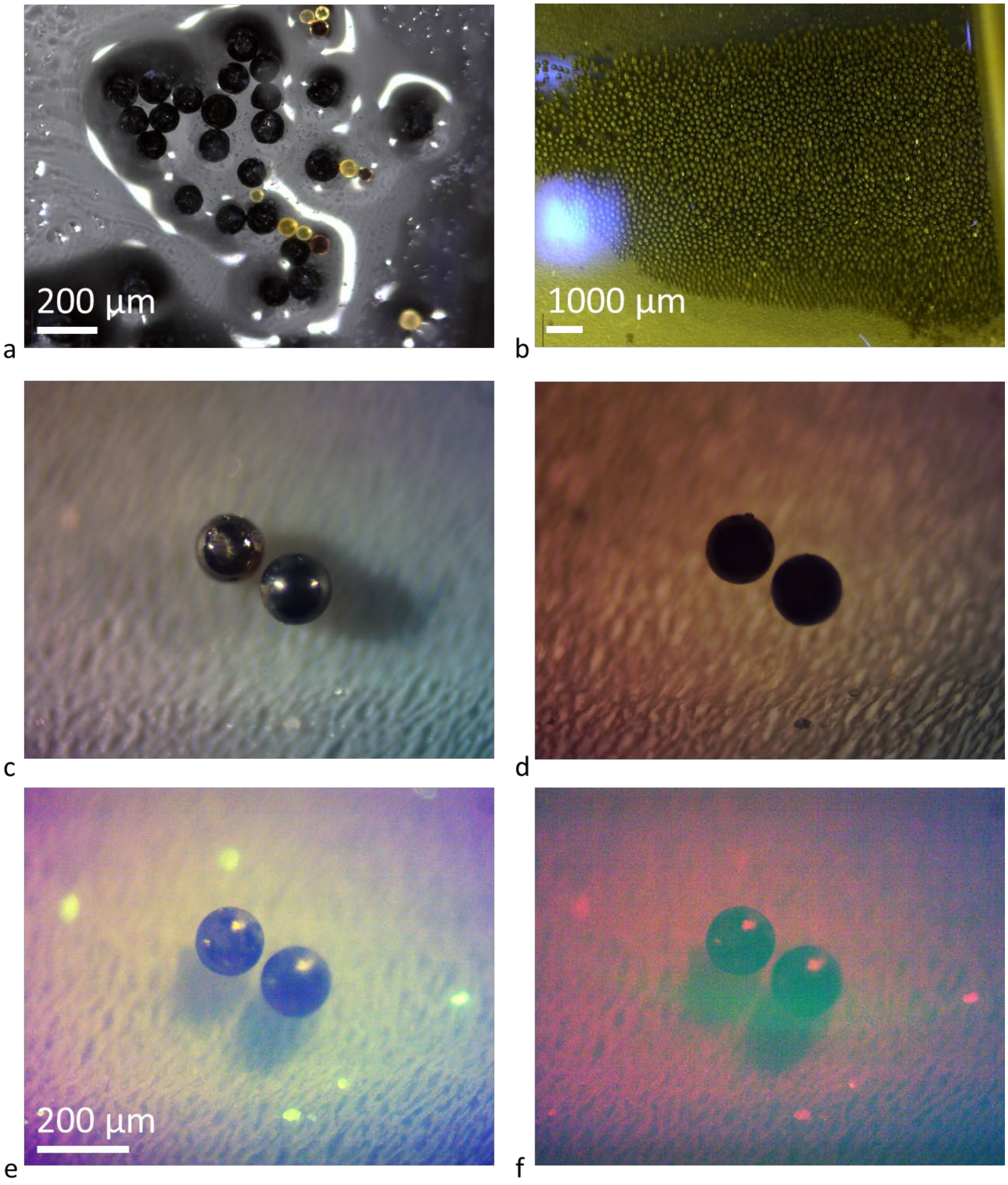

Figure 9 a) Brightfield Micrograph of a Mixture of Ti Plated onto CeO_2 (Dark Spheres) and Uncoated CeO_2 (Green Smaller Spheres) for a Direct In-Image Size Comparison. b) Ambient Light of a Collection of Iridium-Coated Cerium Spheres After Heating at 250°C in a Vacuum for 72 hours. c) A Brightfield Image of the Spheres From (b) Showing the Reflective Aspect of the Coating. d) A Dark Field Image of the Spheres Showing that the Transmission of the Ceria Cores is Completely Occluded by the Coating. e) A UV Micrograph of the Spheres Showing No Salts Present on the Surface of the Coating. f) 600–980 nm Reflectance Micrograph Showing No Oxide Signal From the Coated Spheres.

The calculated shell thickness for each pure metal coating is plotted in Figure 12a. The success of each coating is demarked by a blue title for mixtures of metal and oxide, a black mark for metal coating, and gray if the coating failed and/or destroyed the ceria cores. The atoms of metal added to the sphere compared to the atoms of cerium in the core range from 0.72 to 2.50 with the coatings approaching a 1:1 ratio (~a 15-micron thick shell) until palladium, which is the only metal to exceed a ratio of one. The reduction potential vs. the electronegativity of the metal shows 3 general groups in relation to the core ceria, as shown in Figure 12b.

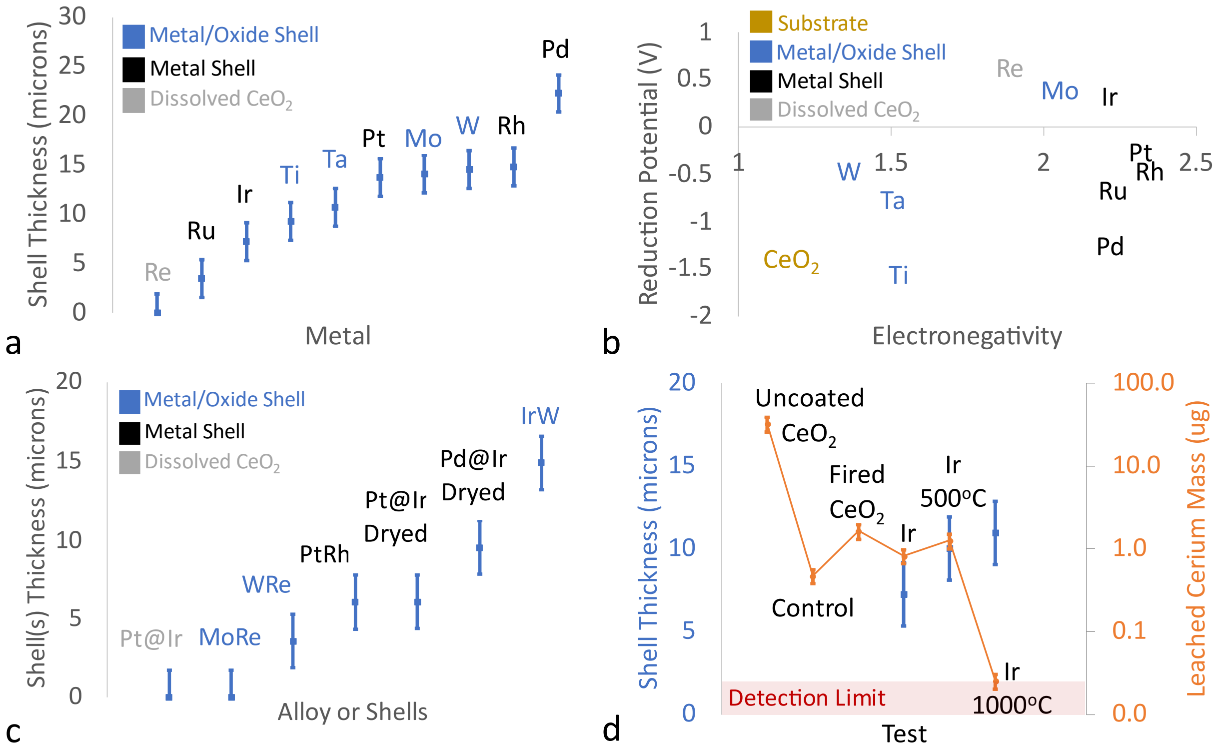

Figure 10 Shell Thickness Determination. a) The Thickness of Each Metallic Shell Color-Coded to the End Chemical State of the Coating. b) The Coating's Reduction Potential Plotted vs. the Electronegativity of the Constituent Atom. c) The Shell Determination of Attempted Alloy Coatings With the End State of the Shell. It Should Be Noted that "Dried" in the Case Title Indicates that the Previous Interlayer Was Dried at 250°C at Vacuum for 72 hrs. d) The Results of the Leaching of Cerium From Dots by Way of 72 hr Ambient Methanol Addition.

With pure metal coatings aligned into groups by successful metal coating, alloys were then tried, and the results are plotted in Figure 12c. Along with alloys (a 1:1 mole ratio was attempted in this work), some subsequent double metal coatings were attempted. Finally, as iridium coating was seen as the most applicable to an accident-tolerant fuel, coated spheres were leach tested before and after firing. The results are presented in Figure 12d.

4.0 Discussion

The process overall was a success in coating ceria oxide microspheres with metal. Generally, the process produces metal films in line with general metal polyol reduction (Hubbard 2016). The final shell thickness equates to 0.7–1 ratio to the mol ratio in all but one case (palladium, data shown in Figure 12a). This reasonably corresponds to the amine:Ce ratio in Figure 9c (0.8–1). Thus, the functionalization with amines saturates the pores of the cerium oxide cores and is used to maximize the metal deposition during the electroless coating process. The metal-to-surface site ratio aligns well with the previously established work in this area (Hubbard 2016). As an approximate check, the amount of metal added to the spheres makes physical sense and appears to correspond to a mechanism where the amine functionalization has coated nearly all the surface area of the pore network within the ceria. This is further corroborated by the fact that the ceria spheres fired to a temperature where their pore networks had closed only contained spotty to no metal coating. Thus, a substrate oxide with a substantial pore network amiable to functionalization is a necessity for the plating mechanism.

The nature of the compositions as analyzed in Figure 9d, Figure 10c and d, and Figure 11c–f suggest that in several cases, the spheres are coated in metal. Evaluation of the metallic properties (such as electronegativity) and the coating reactions reduction potential lead to three distinct groups (shown in Figure 12b):

1) Those coating near the electronegativity of cerium produced only mixtures of metal and oxide (termed “black metal” colloquially)
2) The coatings with an electronegativity of greater than 2.15 (Pauling basis) produced reliable metal coatings
3) Coatings with positive reduction potentials are more complicated to evaluate and require further research.

The metal coatings have a path to explain their coating performance, and the results appear to align with a mechanism needing a pore network in the ceria to provide sufficient electrostatic charge when coating.

Alloy coatings attempted in this work have several conclusions. Generally, alloy coatings were thinner than either of their constituent metals. In all but one case, the presence of a metal/metal oxide coating reaction led to an almost entirely oxide shell (with some cases being optically transmissive). As alloy coating is possible but complicated, double coating was investigated.

The double coating is possible with one key process addition: the necessity to consolidate in a vacuum furnace the primary metal coating before continuing with a second metal coat. Investigations into coating one metal and then directly coating a second ended in the dissolution of the shells and cores entirely. When the first coating had been heated to drive off the solvent at 250°C in a vacuum for 72 hours, the second layer was plated. It should be noted that the second coating is typically only a micron or so thick, as it is difficult to access the amine termination through the primary metal coat. Thus, double layers are possible, but their added complications led to the selection of an iridium metal coat for leach testing.

As the hypothesis of this work was that a ~10 um thick coating could withstand dissolution of the cerium for 72 hours, iridium was evaluated. The controls all leached around 1 microgram of cerium from a standardized mass of spheres (by cerium content). Initially, iridium coating appeared to have half that mass loss, with lower (400°C) firing doing little to influence the rate of dissolution (Figure 12d). Upon firing to 1,000°C, the mass loss of the core was reduced to the detection limit of the ICPMS system. Thus, it has been determined that the metal coatings can, in the case of iridium, provide leach protection to the cerium cores. This evaluation of the leaching data supports the hypothesis of this work.

4.1 Continuation of Lessons Learned & Further Development

What follows are other key takeaways that will influence the success of further development of this coating technique:

- Chloride salts tend to plate thicker and are more repeatable than acetylacetonate (acac)--based metal salts. The one case where this was found to be not applicable was for rhenium (III) chloride, which was not successful, whereas rhenium (III) acac was successful.
- Stir speeds for the solutions during the entire coating process need to be kept between 200 and 400 RPM. Faster stir rates yielded cracked spheres.
- To ensure coverage of all the microspheres, an excess of metal precursor must be used. However, this causes metal particulates to crash out of the solution in addition to the metal layer that forms on the microspheres. For iridium, approximately a 6:1 ratio by weight of microspheres to iridium results in plated particles with a minimal amount of free metal. This ratio should be fine-tuned. It should also be determined for every metal of interest, as the ratios needed are likely not identical.
    - It may not be possible to eliminate the excess metal, only reduce it. A method to separate coated spheres from free metal will need to be developed. Potential methods include:
        - Density-based method: the microspheres should have a different density than the metal particles. Finding the correct liquid to use should cause one group to sink and the other to float. Particles can then either be drained out of the bottom of the vessel or skimmed off the top. This would require a good amount of experimentation to determine the correct liquid to use.
        - Filtration: using a pair of filters of slightly different sizes, narrow the gap of acceptable particle sizes such that metal fragments that are significantly larger or smaller than the plated microspheres are rejected. Some metal particles would stay with the microspheres if they were the correct size. Some microspheres could potentially also be rejected. This is dependent upon being able to find filters that have the necessary pore sizes.
- A cleaning method needs to be developed, particularly before the consolidation (vacuum furnace) step. If the microspheres are consolidated when the plating solution has been decanted off, but not washed, an odd “fuzzy-looking” layer appears that we hypothesize is metal that has crashed out as the plating solution evaporated. Odd metal fragments also form that are visually distinct from the metal fragments that form during the electroless plating step. This possibly dendritic formation is likely to cause poor adhesion in double coatings and could interfere with several of the possible separation methods listed above.

5.0 Conclusion

The deposition of thin, continuous layers of high-temperature, corrosion-resistant metals onto oxide microspheres presents a new range of possibilities for micro-engineered powders for applications such as advanced nuclear fuels and catalysts. The metallic layer presents the possibility to decrease the temperature drop across otherwise low conductivity fuels and also provides a barrier between radioactive materials and the environment. The coating methodology described in this study provides a way to surround fuels in thin metal layers, thus enabling increased thermal conductivity and accident tolerance. Of the coating materials considered, iridium was selected as an attractive coating material for nuclear fuel applications. Experiments were successful in applying coatings of iridium and other candidate materials on cerium oxide microspheres. Additional development is needed to refine and scale processing methods.

6.0 References

Aegerter, M. A., N. Leventis, and M. M. Koebel. 2011. *Aerogels Handbook*. edited by M. A. Aegerter, N. Leventis, and M. M. Koebel. New York, NY: Springer. https://doi.org/10.1007/978-1-4419-7589-8.

Arima, T., K. Idemitsu, K. Yamahira, S. Torikai, and Y. Inagaki. 2005. “Application of internal gelation to sol–gel synthesis of ceria-doped zirconia microspheres as nuclear fuel analogous materials.” *Journal of Alloys and Compounds* 394 (1-2): 271-276. https://doi.org/10.1016/j.jallcom.2004.10.040.

ASM. *Metals Handbook Desk Edition, Second Edition*. ASM Internationl.

Axler, K. M., and D. T. Eash. 1987. *High-Temperature Compatability Study of Iridum (DOP-26 Alloy) with Graphite and Plutonia.* Los Alamos National Laboratory LA-11127-MS.

Brykala, M., and M. Rogowski. 2016. “The Complex Sol–Gel Process for producing small ThO2 microspheres.” *Journal of Nuclear Materials* 473: 249-255. https://doi.org/10.1016/j.jnucmat.2016.03.004.

Carroll, K. J., J. U. Reveles, M. D. Shultz, S. N. Khanna, and E. E. Carpenter. 2011. “Preparation of Elemental Cu and Ni Nanoparticles by the Polyol Method: An Experimental and Theoretical Approach.” *The Journal of Physical Chemistry C* 115 (6): 2656-2664. https://doi.org/10.1021/jp1104196.

Clark, C. R., G. A. Moore, J. F. Jue, B. H. Park, and N. P. Hallinan. 2007. *Update on US High Density Fuel Fabrication Development.* RRFM - Research Reactor Fuel Management. https://www.researchgate.net/publication/242119803_Update_on_US_High_Density_Fuel_Fabrication_Development.

Clavier, N., G. I. N. Bouala, J. Léchelle, J. Martinez, N. Dacheux, and R. Podor. 2017. “Novel approaches for the in situ study of the sintering of nuclear oxide fuel materials and their surrogates.” *Radiochimica Acta* 105 (11): 879-892. https://doi.org/10.1515/ract-2016-2659.

Darling, A. S. 1966. “The Elastic and Plastic Properties of the Platinum Metals.” *Platinum Metals Review* 10 (1): 14-19. https://doi.org/10.1595/003214066x1011419.

Fievet, F., S. Ammar-Merah, R. Brayner, F. Chau, M. Giraud, F. Mammeri, J. Peron, J. Y. Piquemal, L. Sicard, and G. Viau. 2018. “The polyol process: a unique method for easy access to metal nanoparticles with tailored sizes, shapes and compositions.” *Chem Soc Rev* 47 (14): 5187-5233. https://doi.org/10.1039/c7cs00777a.

Garcia, J. R. V., and T. Goto. 2003. “Chemical Vapor Deposition of Iridium, Platinum, Rhodium and Palladium.” *Materials Transactions* 44 (9): 1717-1728. https://doi.org/10.2320/matertrans.44.1717.

Hao, S., J. Ma, X. Zhao, Y. Wang, X. Zhou, and C. Deng. 2014. “Large-scale production of UO2 kernels by sol–gel process at INET.” *Nuclear Engineering and Design* 271: 158-161. https://doi.org/10.1016/j.nucengdes.2013.11.025.

Harp, J. M., P. A. Lessing, and R. E. Hoggan. 2015. “Uranium silicide pellet fabrication by powder metallurgy for accident tolerant fuel evaluation and irradiation.” *Journal of Nuclear Materials* 466: 728-738. https://doi.org/10.1016/j.jnucmat.2015.06.027.

Hubbard, L. 2016. “Electrostatic Coating with Charge-Compensated Ligandless Copper Nanoparticles.” Doctor of Philosopy with a Major in Chemical Engineering, A Dissertation Submitted to the Faculty of the Department of Chemical and Environmental Engineering, The University of Arizona. https://repository.arizona.edu/handle/10150/612398.

Katalenich, J., and J. Sholtis. 2021. “Microsphere Plutonium-238 Oxide Fuel to Revolutionize New Radioisotope Power Systems and Heat Sources for Planetary Exploration.” *Bulletin of the AAS* 53 (4). https://doi.org/10.3847/25c2cfeb.bd33466c.

Katalenich, J. A. 2017. "Production of cerium dioxide microspheres by an internal gelation sol–gel method." *Journal of Sol-Gel Science and Technology* 82 (3): 654-663. https://doi.org/10.1007/s10971-017-4345-8.

Katalenich, J. A., B. B. Kitchen, and B. D. Pierson. 2018. "Production of monodisperse cerium oxide microspheres with diameters near 100 µm by internal-gelation sol–gel methods." *Journal of Sol-Gel Science and Technology* 86 (2): 329-342. https://doi.org/10.1007/s10971-018-4641-y.

Klopp, W. D. 1985. "Technology status of molybdenum and tungsten alloys." *Space nuclear power systems 1984 proceedings* 2.

Luo, A., J. J. Park, L. Jacobson, B. H. Tsao, and M. S. Ramalingam. 1994. "High-Temperature Tensile Properties of a Molybdenum-5%Rhenium-0.5% Hafnium Carbide Alloy." In *AIP Conference Proceedings* 301 (1): 421–426. Space Nuclear Power and Propulsion: Eleventh Symposium, Albuquerque, New Mexico. https://doi.org/https://doi.org/10.1063/1.2950211.

Lyon, S. B. 2010. "3.21 - Corrosion of Noble Metals." *Shreir's Corrosion* 3: 2205-2224. https://doi.org/https://doi.org/10.1016/B978-044452787-5.00109-8.

Ma, H., H. Wang, P. C. Burns, B. K. McNamara, E. C. Buck, and C. Na. 2016. "Synthesis and preservation of graphene-supported uranium dioxide nanocrystals." *Journal of Nuclear Materials* 475: 113-122. https://doi.org/10.1016/j.jnucmat.2016.03.027.

Maji, D., K. Ananthasivan, R. V. Krishnan, S. Balakrishnan, B. Kothandaraman, G. Jogeswararao, A. Senapati, R. Padmanabhan, B. A. Kumar, S. Balasubramonian, and V. Jayaraman. 2023. "A gelation facility for the preparation of ceramic microspheres." *Progress in Nuclear Energy* 162. https://doi.org/10.1016/j.pnucene.2023.104769.

Matthews, R. B., and P. E. Hart. 1980. "Nuclear fuel pellets fabricated from gel-derived microspheres." *Journal of Nuclear Materials* 92 (2-3): 207-216. https://doi.org/10.1016/0022-3115(80)90104-x.

Morris. 1978. US Patent 4111718.

Park, S., M. Park, P. Han, and S. Lee. 2006. "The Effect of pH-adjusted Gold Colloids on the Formation of Gold Clusters over APTMS-coated Silica Cores." *Bulletin of the Korean Chemical Society* 27 (9): 1341-1345. https://doi.org/10.5012/bkcs.2006.27.9.1341.

Schneibel, J. H., R. G. Miller, C. A. Carmichael, E. E. Fox, G. B. Ulrich, and E. P. George. 2017. *HIgh Strain Rate Tensile Properties of Welded DOP-26 Iridium.* Oak Ridge National Laboratory ORNL/TM-2017/276. https://info.ornl.gov/sites/publications/Files/Pub75110.pdf.

Shapley, J. R., W. S. Uchiyama, and R. A. Scott. 2002. "Bimetallic catalysts from alumina-supported molybdenum-iridium clusters." *The Journal of Physical Chemistry* 94 (3): 1190-1196. https://doi.org/10.1021/j100366a035.

Sökücü, A. S., M. Bedir, and M. T. Aybers. 2015. "Study on Preparation and First-Stage Sintering Kinetics of ThO2-UO2Pellets Made by Sol-Gel Microspheres Technique." *Acta Physica Polonica A* 127 (4): 987-991. https://doi.org/10.12693/APhysPolA.127.987.

Somayajulu, P. S. 2017. "Synthesis and Characterization of Coated Agglomerate Pelletisation (CAP) Pellets of Thoria Based Materials for Nuclear Fuels." Doctor of Philosophy, Board of Studies in Engineering Sciences, Homi Bhabha National Institute (ENGG 01200904023). http://www.hbni.ac.in/phdthesis/engg/ENGG01200904023.pdf.

Song, B., K. Nelson, R. Lipinski, J. Bignell, G. B. Ulrich, and E. P. George. 2015. High-Temperature Mechanical Properties of a DOP-26 Iridium Alloy under Impact Loading. Sandia National Laboratories,. https://anstd.ans.org/wp-content/uploads/2015/07/5001_Song-et-al.pdf.

Suresh Kumar, K., H. P. Nawada, and N. P. Bhat. 2003. "Comparative study of thermal decomposition of the sol–gel products of U and Ce by external and internal gelation processes." *Journal of Nuclear Materials* 321 (2-3): 263-268. https://doi.org/10.1016/s0022-3115(03)00278-2.

Tietz, T. E., and W. J. Wilson. 1961. *Final Report: Mechancial, Oxidation, and Thermal Property Data for Seven Refractory Metals and Their Alloys.* https://apps.dtic.mil/sti/tr/pdf/AD0266824.pdf.

Tsoulfanidis, N., and S. Landsberger. 1995. "Measurement & Detection of Radiation, 2nd Edition." *Scientific Research: An Academic Publisher*.

Yo, C. Y., R. W. Powell, and P. E. Liley. 1974. "Thermal Conductivity of the Elements: A Comprehensive Review." *Journal of Physical and Chemical Reference Data* 3, no. 1.

7.0 Bibliography

ASM International. 1998. “Refractory Metals and Alloys.” In *Metals Handbook Desk Edition*, 629–633. https://doi.org/10.31399/asm.hb.mhde2.a0003151 .

Burkes, D. E., R. S. Fielding, D. L. Porter, M. K. Meyer, and B. J. Makenas. 2009. “A US perspective on fast reactor fuel fabrication technology and experience. Part II: Ceramic fuels.” *Journal of Nuclear Materials* 393 (1): 1–11. https://doi.org/10.1016/j.jnucmat.2009.04.023.

Clark, C. R., G. A. Moore, J. F. Jue, B. H. Park, N. P. Hallinan, D. M. Wachs, and D. E. Burkes. 2007. *Update on US High Desnity Fuel Fabrication Development: Research Reactor Fuel Management (RRFM)*. INL/CON-07-12355. https://inldigitallibrary.inl.gov/sites/sti/sti/3628664.pdf .

Costa, D. R., M. Hedberg, S. C. Middleburgh, J. Wallenius, P. Olsson, and D. A. Lopes. 2020. “UN microspheres embedded in UO2 matrix: An innovative accident tolerant fuel.” *Journal of Nuclear Materials* 540. https://doi.org/10.1016/j.jnucmat.2020.152355.

CRC. 1987. *Handbook of Chemistry and Physics*, 95th Edition. Boca Raton, FL: CRC Press, Taylor & Francis Group.

Hartanto, D., Y. Kim, and F. Venneri. 2015. “Neutronics evaluation of a super-deep-burn with TRU Fully Ceramic Microencapsulated (FCM) fuel in CANDU.” *Progress in Nuclear Energy* 83: 261–269. https://doi.org/10.1016/j.pnucene.2015.04.001.

Hunt, R. D., J. L. Collins, M. H. Lloyd, and S. C. Finkeldei. 2019. “Production of more ideal uranium trioxide microspheres for the sol-gel microsphere pelletization process without the use of carbon.” *Journal of Nuclear Materials* 515: 107–110. https://doi.org/10.1016/j.jnucmat.2018.12.029.

Katalenich, J. A. 2019. “Impurity levels in cerium oxide microspheres prepared by internal gelation sol–gel methods.” *Journal of Sol-Gel Science and Technology* 94 (3): 596–606. https://doi.org/10.1007/s10971-019-05165-2.

Korean Chemical Society. 2006. “The Effect of pH-adjusted Gold Colloids on the Formation of Gold Clusters over APTMS-coated Silica Cores.” *Bulletin of the Korean Chemical Society* 27 (9): 1341–1345. https://doi.org/10.5012/bkcs.2006.27.9.1341.

Kumar, N., Y. R. Bamankar, K. T. Pillai, S. K. Mukerjee, V. N. Vaidya, and V. Venugopal. 2006. “Effect of feed solution composition and heat treatment conditions on the morphology of uranium oxide microspheres prepared by sol–gel process.” *Journal of Nuclear Materials* 359 (1-2): 80-92. https://doi.org/10.1016/j.jnucmat.2006.07.019.

Lee, W. E., M. Gilbert, S. T. Murphy, R. W. Grimes, and D. J. Green. 2013. “Opportunities for Advanced Ceramics and Composites in the Nuclear Sector.” *Journal of the American Ceramic Society* 96 (7): 2005–2030. https://doi.org/10.1111/jace.12406.

Lee, Y.-W., J.-Y. Park, Y. K. Kim, K. C. Jeong, W. K. Kim, B. G. Kim, Y. M. Kim, and M. S. Cho. 2008. “Development of HTGR-coated particle fuel technology in Korea.” *Nuclear Engineering and Design* 238 (11): 2842–2853. https://doi.org/10.1016/j.nucengdes.2007.11.023.

Li, S., J. Bai, S. Cao, X. Yin, C. Tan, P. Li, W. Tian, J. Wang, H. Guo, and Z. Qin. 2018. “An improved internal gelation process without cooling the solution for preparing uranium dioxide ceramic microspheres.” *Ceramics International* 44 (2): 2524–2528. https://doi.org/10.1016/j.ceramint.2017.11.001.

Lu, C., T. Koyanagi, Y. Katoh, G. Strydom, K. A. Terrani, and N. R. Brown. 2019. “Fully Ceramic Microencapsulated fuel in prismatic high-temperature gas-cooled reactors: Sensitivity of reactor behavior during design basis accidents to fuel properties and the potential impact of the SiC defect annealing process.” *Nuclear Engineering and Design* 345: 125–147. https://doi.org/10.1016/j.nucengdes.2019.02.012.

Qasim Awan, M., L. Cao, and H. Wu. 2017. “Neutronic design and evaluation of a PWR fuel assembly with accident tolerant-Fully Ceramic Micro-Encapsulated (AT-FCM) fuel.” *Nuclear Engineering and Design* 319: 126–139. https://doi.org/10.1016/j.nucengdes.2017.04.019.

Raftery, A. M., R. L. Seibert, D. R. Brown, M. P. Trammell, A. T. Nelson, and K. A. Terrani. 2020. “Fabrication of UN-Mo CERMET Nuclear Fuel Using Advanced Manufacturing Techniques.” *Nuclear Technology* 207 (6): 815–824. https://doi.org/10.1080/00295450.2020.1823187.

Sawant, R. M., N. K. Chaudhuri, and K. L. Ramakumar. 2002. *Journal of Radioanalytical and Nuclear Chemistry* 252 (3): 485–489. https://doi.org/10.1023/a:1015842401768.

Schneibel, J. H., R. G. Miller, C. A. Carmichael, E. E. Fox, G. B. Ulrich, and E. P. George. 2017. *High Strain Rate Tensile Properties of Welded DOP-26 Iridium*. Oak Ridge National Laboratory ORNL/TM-2017/276. https://info.ornl.gov/sites/publications/Files/Pub75110.pdf.

Sodd, D. D. 2010. “The role sol-gel process for nuclear fuels--an overview.” *J Sol-Gel Sci Technology* 59: 404–416. https://doi.org/https://doi.org/10.1007/s10971-010-2273-y.

Song, B., K. Nelson, R. Lipinski, J. Bignell, G. B. Ulrich, and E. P. George. 2015. *High-Temperature Mechanical Properties of a DOP-26 Iridium Alloy under Impact Loading*. Sandia National Laboratories. https://anstd.ans.org/wp-content/uploads/2015/07/5001_Song-et-al.pdf.

Sukarsono, R., M. Rachmawati, S. R. Susilowati, D. Husnurrofiq, K. Nurwidyaningrum, and A. K. Dewi. 2018. “Effect of Sol Concentration, Aging and Drying Process on Cerium Stabilization Zirconium Gel Produced by External Gelation.” *Journal of Physics: Conference Series* 962: 012056.

The University of Arizona. n.d. “Electrostatic Coating with Charge-Compensated Ligandless Copper Nanoparticles.” https://repository.arizona.edu/handle/10150/612398?show=full.

Tsoulfanidis, N., and S. Landsberger. 1995. “Measurement & Detection of Radiation, 2nd Edition.” *Scientific Research: An Academic Publisher*.

Tummalapalli, M.K., et al., *Evaluation of thermophysical properties of UO2-10 Vol% Mo nuclear fuel pellets.* Journal of Nuclear Materials, 2022. **559**.

Ueta, S., J. Aihara, K. Sawa, A. Yasuda, M. Honda, and N. Furihata. 2011. “Development of high temperature gas-cooled reactor (HTGR) fuel in Japan.” *Progress in Nuclear Energy* 53 (7): 788-793. https://doi.org/10.1016/j.pnucene.2011.05.005.

Vaidya, V. N., S. K. Mukherjee, J. K. Joshi, R. V. Kamat, and D. D. Sood. 1987. “A study of chemical parameters of the internal gelation based sol-gel process for uranium dioxide.” *Journal of Nuclear Materials* 148 (3): 324–331. https://doi.org/10.1016/0022-3115(87)90026-2.

Xiangwen, Z., L. Zhenming, Z. Jie, L. Bing, Z. Yanwen, T. Chunhe, and T. Yaping. 2013. “Preparation of spherical fuel elements for HTR-PM in INET.” *Nuclear Engineering and Design* 263: 456–461. https://doi.org/10.1016/j.nucengdes.2013.07.001.

Pacific Northwest
National Laboratory

902 Battelle Boulevard
P.O. Box 999
Richland, WA 99354

1-888-375-PNNL (7665)

www.pnnl.gov